JOURNAL OF THE ROYAL SOCIETY Interface

rsif.royalsocietypublishing.org

Research

Cite this article: Gillies AG, Fearing RS. 2014 Simulation of synthetic gecko arrays shearing on rough surfaces. *J. R. Soc. Interface* **11**: 20140021.
http://dx.doi.org/10.1098/rsif.2014.0021

Received: 8 January 2014
Accepted: 12 March 2014

Subject Areas:
biomechanics, biomimetics

Keywords:
bioinspired adhesion, gecko, friction, shear, sliding

Author for correspondence:
Andrew G. Gillies
e-mail: andrew.gillies@berkeley.edu

Royal Society Publishing

Simulation of synthetic gecko arrays shearing on rough surfaces

Andrew G. Gillies[1] and Ronald S. Fearing[2]

[1]Department of Mechanical Engineering, and [2]Department of Electrical Engineering and Computer Sciences, University of California, Berkeley, CA 94720, USA

To better understand the role of surface roughness and tip geometry in the adhesion of gecko synthetic adhesives, a model is developed that attempts to uncover the relationship between surface feature size and the adhesive terminal feature shape. This model is the first to predict the adhesive behaviour of a plurality of hairs acting in shear on simulated rough surfaces using analytically derived contact models. The models showed that the nanoscale geometry of the tip shape alters the macroscale adhesion of the array of fibres by nearly an order of magnitude, and that on sinusoidal surfaces with amplitudes much larger than the nanoscale features, spatula-shaped features can increase adhesive forces by 2.5 times on smooth surfaces and 10 times on rough surfaces. Interestingly, the summation of the fibres acting in concert shows behaviour much more complex that what could be predicted with the pull-off model of a single fibre. Both the Johnson–Kendall–Roberts and Kendall peel models can explain the experimentally observed frictional adhesion effect previously described in the literature. Similar to experimental results recently reported on the macroscale features of the gecko adhesive system, adhesion drops dramatically when surface roughness exceeds the size and spacing of the adhesive fibrillar features.

1. Introduction

The variety of surfaces found in nature pose a formidable challenge to any adhesive system. Often, these surfaces have roughnesses at a variety of length scales, ranging from nanometres to large undulations on the centimetre scale. These roughnesses can be critical, as it has been shown that just a few nanometres in roughness is enough to disrupt the adhesion between clean elastically hard surfaces [1], and that a root mean square roughness of only 1 µm is enough to completely remove the adhesion between a soft rubber with a Young's modulus of 1 MPa and a hard flat substrate [2].

The majority of recent studies on the gecko adhesive system and work on gecko synthetic adhesives (GSAs) have focused on nanoscale roughness or on smooth surfaces, with several notable exceptions [2–9]. However, an integrated approach should consider the relationship between the surface roughness, the size of the adhesive structures and their ability to conform at a variety of length scales [10,11]. Understanding the abilities and limitations of these structures on varying length scales of roughness is necessary to create an adhesive that is able to adhere to naturally rough surfaces.

Below, we develop a model that examines the shear and normal adhesive properties of an array of microfibres while being dragged across surfaces of varying roughness. We consider two fibre tip geometries: those with hemispherical-tipped terminal features and those with spatula-shaped terminal features. To the best of the authors' knowledge, this model is the first to predict the adhesive behaviour of a plurality of hairs acting in shear on simulated rough surfaces using analytically derived contact models.

There are many examples in the literature of gecko fibre models that describe the adhesive properties of an individual fibre through varying fibre tip shape [12–15], fibre dimensions [16], contribution of capillary forces [17] or robustness to roughness [18,19], most of which model the fibres as elastic beams [10,20–23]. There are fewer examples of models that describe how an

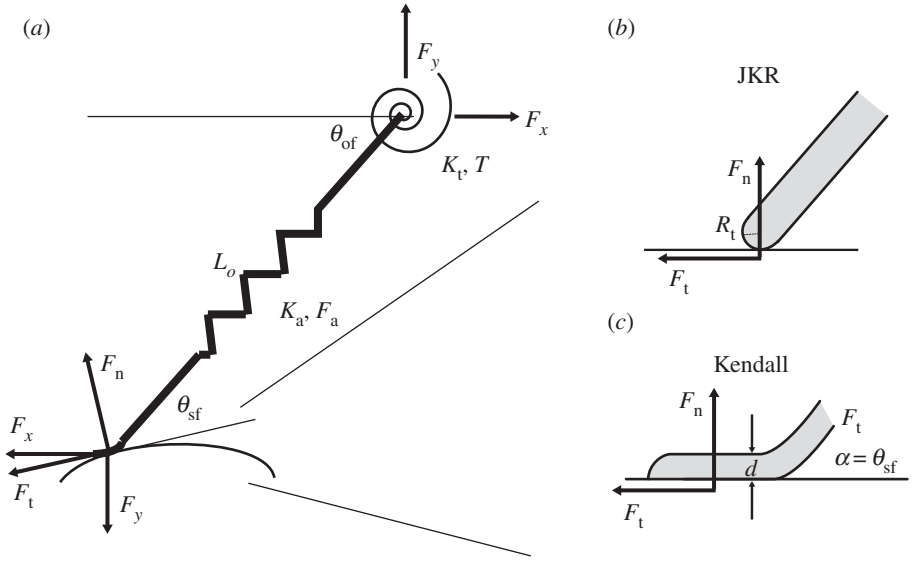

Figure 1. (*a*) Modelled approximation of the fibre and the relevant parameters indicated. The fibre is modelled with an axial spring and a torsional spring at its base that approximates fibre bending with a pseudo-rigid body model [34]. (*b*) Hemispherical tips approximated by the JKR contact model and (*c*) spatula tips approximated by the Kendall peel model.

array of fibres work together in concert to give rise to adhesive forces across the total array, which on rough surfaces will be different than just a scaled version of the adhesive forces generated by a single fibre [24,25]. Some of these models consider several hierarchical levels [4,7,26,27], and some consider shear on smooth or spherical indenters with a frictional adhesion cantilever or curved beam model [20,28]. Another study examines a logarithmic fit to experimental data to explain how the uncorrelated stick–slip behaviour of fibres sliding on a surface gives rise to velocity dependence [29,30]. However, there have been no examples of models that include shearing of the array and attempt to capture the coupling between the shear adhesion and normal adhesion on rough surfaces across an array of fibres. The model below describes the load–drag–pull (LDP) style of GSA testing that is becoming widely accepted in the literature [31–33].

2. Fibre model assumptions

As in many examples cited above, the fibres are modelled as spring elements approximated by a rotational spring at the base and a linear spring along the length of the fibre (figure 1). These spring elements approximate the bending of the fibre by rotational stiffness, K_t, and axial stiffness of the fibre, K_a, which constitutes a pseudo-rigid body model of the fibre and simplifies the numerical calculation, as carried out by Schubert *et al.* [20] and Tian *et al.* [35]. Howell [34] describes that the bending of a thin elastic beam can be approximated for large deflections as a torsional spring with stiffness

$$K_t = \frac{\pi \phi E_{fibre} I}{L_o}, \tag{2.1}$$

where ϕ is a characteristic radius factor ($\phi \approx 0.82$ for this case), E_{fibre} is the Young's modulus of the fibre material, L_o is the initial fibre length and I is the second moment of inertia of the fibre, which in the case of a circular fibre cross section is $\pi r_f^4/4$, where r_f is the fibre radius. The axial stiffness of the fibre is

$$K_a = \frac{\pi r_f^2 E_{fibre}}{L_o}. \tag{2.2}$$

The assumption for both the axial stiffness and the bending stiffness is made that the change in fibre length does not significantly affect the stiffness of the structure. As shown in figure 1, the fibre is prescribed an initial angle, θ_{of}, and the angle at each simulation step is calculated as $\theta_{current} = \tan^{-1}((y_{tip} - y_{root})/(x_{tip} - x_{root}))$. Forces acting on the fibre at the tip in the shear direction and normal direction are F_x and F_y, respectively. Forces are calculated by first determining the displacement of the fibre tip from its initial rest configuration, and then calculating the axial force $F_A = K_a * (L_{current} - L_o)$ and the torsional force $F_{tor} = K_t * (\theta_{current} - \theta_{of})/L_{current}$. These are then used to calculate F_x and F_y via a rotation:

$$\left.\begin{aligned} F_x &= F_A \cos(\theta_{current}) + F_{tor} \sin(\theta_{current}) \\ F_y &= F_A \sin(\theta_{current}) - F_{tor} \cos(\theta_{current}). \end{aligned}\right\} \tag{2.3}$$

The backing connecting the fibres is assumed to be rigid, and supports the fibres spaced at a constant pitch. The total shear and normal adhesive forces for the array are taken as the sum of the individual fibre shear and normal forces.

Dimensions and material properties of the fibres are chosen based on the stiff thermoplastic fibres used in Schubert *et al.* [20], Lee *et al.* [8] and Gillies *et al.* [36] and outlined in table 1. Uncorrelated stick slip behaviour was achieved numerically by randomly assigning each hair an initial inclination angle and length that were commensurate with observations of the aforementioned fabricated arrays. Based on fibre measurements, the fibre length is 18.5 ± 1.5 µm (uniform distribution) and the angle varies by $\pm 5^\circ$ (uniform distribution). Furthermore, interfibre collision and adhesion is neglected. Although interfibre compaction likely becomes significant under high loads in the natural gecko [11,36], a previous simulation of a GSA which neglected interfibre collision showed reasonable agreement with experiment [20]. The simulation was run with an array of 250 hairs, because this number was large enough to make an individual hair contribution significantly small if all hairs were in contact (less than 1%).

Table 1. Fibre properties used for simulation.

property	dimension
Young's modulus	1 GPa
fibre radius	300 nm
length	18.5 μm
pitch	3 μm
adhesion energy	30 mJ m^{-2}
tip radius	150 nm
spatula width	200 nm
spatula thickness	10 nm

3. Surface characterization and load–drag–pull path

For the model, two contact surface types are considered: a spherical probe with a radius of 2 cm and a sinusoidal surface with amplitude A and wavelength λ. For each surface, the profile is discretized into an array of $x_{surface}$ and $y_{surface}$ coordinates, with a spacing of $e = 5 \times 10^{-9}$ m. The spherical indenter size is chosen so that, at full indentation, the array spans beyond the width of the indenter, as would be the case for a macroscopic adhesion measurement. For the sinusoidal surface, amplitudes and wavelengths are chosen to be of the same size order as the fibre length and spacing. Sinusoidal surfaces are chosen so that the effect of varying 'asperity' sizes can be studied in a systematic way by isolating feature sizes through amplitude and wavelength. This type of isolation would not be possible with a randomly generated rough surface.

Owing to the coupling of normal and tangential adhesive forces exhibited in the gecko adhesive system, it is important that any testing methodology selected is able to capture this interplay by allowing measurement in more than a single axis. In the past several years, the LDP testing methodology has emerged as a repeatable methodology that is useful for both natural and synthetic systems [31–33]. LDP testing involves moving the sample through a displacement-controlled path which brings the sample into contact with a counter-surface, whereas reaction forces are measured in each axis. Owing to the controllability and repeatability of this displacement-controlled methodology, and its adoption by many other GSA investigators, the LDP test was used for this study. However, important considerations must be taken when interpreting the results of the LDP test. Owing to the displacement-controlled nature of the LDP test, it is not directly relevant to map the results to systems and applications that have different boundary conditions. For example, in the case of a robot climbing a wall, the path of the robot body is dictated by the forces acting on the system, and it can be considered a force-controlled system. In a force-controlled system, a load will be applied to the adhesive, and if this load does not exceed the adhesive limit, contact will be maintained. This is in contrast to the displacement-controlled LDP system, where the adhesive will be driven past this failure point, but the path will still be followed, allowing the adhesive to possibly re-engage. We therefore generally report either the maximum adhesive forces during an LDP trial, or the mean forces during the drag phase of a trial, because this could approximately be considered the adhesion limits of the system that one might expect during applications with different boundary conditions.

LDP path generation consists of three phases: a loading phase where the surface approaches the array on a fixed path at an angle of 45° to the surface, for a distance of 25 μm; immediately following loading, the surface is dragged parallel to the fibre array for a distance of 10 μm; and finally during the unloading phase the surface moves away from the array at an angle of 45° for a distance of 25 μm (figure 2). For each LDP path, the surface indents into the fibre array a fixed displacement, Δ.

4. Fibre tip contact

To better understand the influence of tip geometry on the adhesion of an array of microfibres, we model the fibre tip using two different geometries. First, we model the fibre tips as elastic hemispheres using the well-known Johnson–Kendall–Roberts (JKR) contact model, and second, we model the fibre tips as plates (similar to the gecko's terminal spatula) that peel as a thin tape following the Kendall peel model.

4.1. Johnson–Kendall–Roberts contact model

Hemispherical-tipped fibre modelled using the JKR theory of contact adhesion has been effective for predicting adhesive forces between elastic bodies [16,20,26,37–39]. The fabrication of stiff thermoplastic arrays of microfibres has been largely limited to hemispherical-tipped fibres, and therefore we use the JKR model to estimate the adhesive properties of this design. According to the JKR theory, an elastic sphere, when pressed against a rigid substrate with a force F_n will develop a true contact area with the surface governed by the following equation [40]:

$$A_t(F_n) = \pi\left\{\frac{3(1-\upsilon^2)}{4E}\left(-F_n + 3\pi W_{ad}R_t + \sqrt{-6\pi F_n W_{ad}R_t + (3\pi W_{ad}R_t)^2}\right)\right\}^{2/3}, \quad (4.1)$$

where R_t is the tip radius, υ is Poisson's ratio and W_{ad} is the work of adhesion (approx. 30 mJ m^{-2} for a hard thermoplastic such as polypropylene on glass [41]). Equation (4.1) is linearized about $F_n = 0$, and the tangential force F_t is expressed as a function of the normal force as carried out by Schubert *et al.* [20]:

$$\begin{aligned} F_t &= \pm\, \tau A_t(F_n) \\ &\approx \tau\left[A_t(F_n = 0) + \frac{dA_t(F_n = 0)}{dF_n}F_n\right] \\ &\approx \mu(F_o + F_n), \end{aligned} \quad (4.2)$$

where τ is the interfacial shear strength, $F_o = (9/2)\pi R_t W_{ad}$ is the assumed adhesive component of the contact and $\mu = \tau(d/dF_n)A_t(F_n = 0) \approx 0.2$. As the fibre reaches this F_t limit, we assume that the fibre remains in contact with the surface, but that the fibre slides in shear opposite to the direction of the shear force. In addition, a maximum pull-off force can be calculated, using the same sphere-on-flat assumption, and is given as $F_{JKR} = (3/2)\pi R_t W_{ad}$. This is the maximum normal load a fibre can sustain before detaching completely from the surface [40]. These equations constitute the adhesion

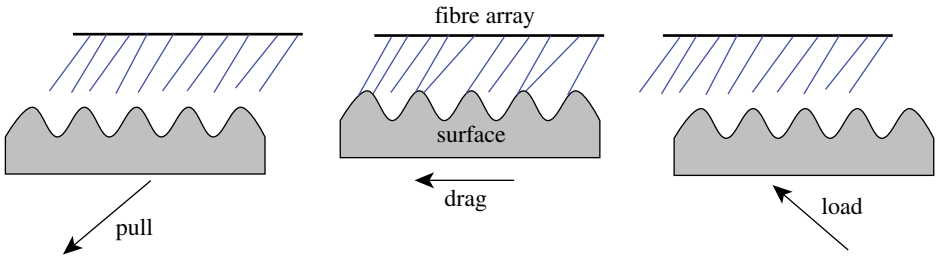

Figure 2. Illustration of the load–drag–pull path. (Online version in colour.)

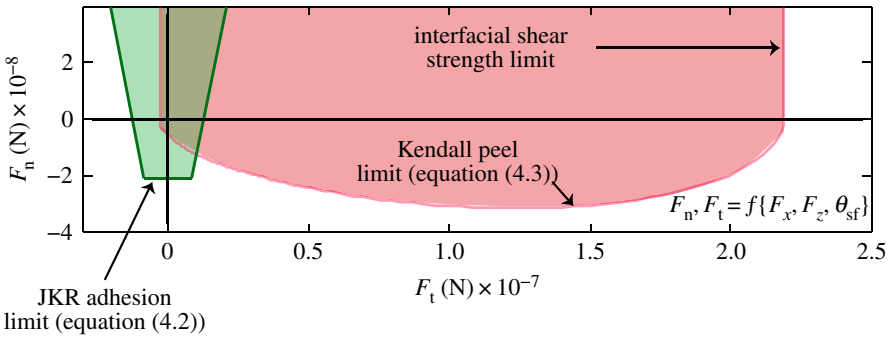

Figure 3. Adhesion limits for both the JKR model as well as the Kendall peel model represented as forces normal (F_n) and tangential (F_t) to the surface. A fibre undergoing axial strain and bending as outlined previously will fall within this force space as a function of the shear and normal load on the fibre, F_x and F_y, as well as the local surface angle, θ_{sf}. Fibres will remain in contact for the forces within the adhesion envelope. Fibre properties and dimensions are given in table 1. (Online version in colour.)

limit for a hemispherical shape tip, beyond which the fibre will either slide or detach as discussed.

4.2. Kendall peel model

It has been hypothesized by many investigators studying the gecko adhesive system, and other biological adhesive systems such as tree frogs [42] that the terminal spatula plates can be modelled as a continuum adhesive surface on a flexible strip that follows Kendall peeling mechanics and is governed by the peeling force [43] as formulated by [31,32]:

$$F = bdE\left(\cos\alpha - 1 + \sqrt{\cos^2\alpha - 2\cos\alpha + 1 + 2R/dE}\right), \quad (4.3)$$

where b is the width of the strip, d is the thickness of the strip, E is the Young's modulus of the strip material, R is the adhesion energy per area and $\alpha = \theta_{sf}$ is the peel angle, which in this case is the angle between the fibre shaft and the surface: the difference between the current fibre angle and the local surface angle where the fibre is making contact, $\theta_{sf} = \theta_{current} - \theta_{local}$. Maximum and minimum peeling forces can be predicted at the limits of the peel angle, with the maximum peel force occurring at $\alpha = 0^\circ$, being $F_{max} = \sqrt{2Rb^2dE}$.

These equations approximate an adhesion limit beyond which the contacting terminal will either slide if normal forces are compressive or detach from the surface via peeling if normal forces are tensile. Although digital hyperextension exhibited by the gecko during detachment could be explained by detachment via a Kendall peel model, whole array forces do not represent Kendall peel behaviour [31,32]. However, it is still unclear whether or not such a model applied to the individual elements would sum to the observed macroscopic behaviour. Our model attempts to predict the cumulative effect of an array of fibres each acting independently.

Adhesion limits are shown in figure 3. A fibre undergoing axial strain and bending will fall within this force space as a function of the shear and normal load on the fibre, F_x and F_y, as well as the local surface angle, θ_{sf}. Fibres will remain in contact as long as the forces are within the adhesion envelope.

5. Numerical simulation

The numerical simulation runs as a displacement-controlled system in which the surface is moved along the LDP path in increments of $i = 10^{-8}$ m, in a quasi-static manner. As the system evolves, each fibre can switch between five possible contact modes: no contact (mode 0), stable tip contact (mode 1), sliding contact (mode 2), detaching contact (mode 3) and side contact (mode 4). A snapshot of the simulation being run on a sinusoidal surface is shown in figure 4.

For a fibre in no contact (mode 0), at each step, it is possible for the fibre to switch into stable tip contact (mode 1), or side contact (mode 4). At each step, a contact detection algorithm is used to determine if each fibre is in contact. Contact can either occur along the length of the fibre (side contact) or at the tip. A linear approximation of the fibre deformation between the fibre root and the fibre tip is used to determine whether any portion of the surface interferes with the fibre through the following equation:

$$\left.\begin{aligned} a &= \frac{y_{tips} - y_{roots}}{x_{tips} - x_{roots}} \\ b &= y_{tips} - a \cdot x_{tips} \\ \delta &= (a \cdot x_{surface} + b) - y_{surface}. \end{aligned}\right\} \quad (5.1)$$

The resulting array, δ, is the vertical distance between the fibre and the surface at each point of the surface array $x_{surface}$. For the elements of δ, tip contact occurs when the first element is found to be negative, and side contact occurs when elements between the second and last are found to be negative.

For a fibre in stable tip contact (mode 1), the fibre tip is stable in its adhered position on the surface at an index n,

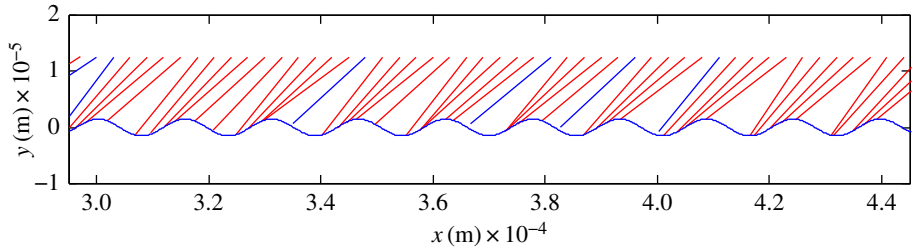

Figure 4. A snapshot of the simulation running on a sinusoidal surface. Fibres in red are in contact, fibres in blue are out of contact. (Online version in colour.)

which identifies its location in space by the previously defined surface: $x_{\text{tip}} = x_{\text{surface}}(n)$ and $y_{\text{tip}} = y_{\text{surface}}(n)$. The force on the base of each fibre is then calculated as described in equations (2.1) and (2.2) using the torsional stiffness, K_t, axial stiffness, K_a, and the transformation described in equation (2.3). These forces are then used in conjunction with the adhesion limit models discussed in §§4.1 and 4.2 to determine whether the fibre will remain in stable tip contact (mode 1), or if it will cross the adhesion limit by sliding (mode 2) or detachment (mode 3). Furthermore, axial compressive loads are limited by Euler buckling, where $F_{A_{\max}} \leq \pi^2 EI/(kL)^2$, where k is a characteristic factor determined by the beam boundary conditions, in this case assumed to be $k = 0.69$ for a pinned–clamped beam. As well, contact detection is once again used to determine whether the fibre will enter into side contact (mode 4).

For a fibre entering into sliding contact (mode 2), the fibre is assumed to remain in contact with the surface, and translate in the direction opposite of the shear force on the fibre, $x_{\text{tip}} = x_{\text{surface}}(n - 1 \times \text{sgn}(F_x))$ and $y_{\text{tip}} = y_{\text{surface}}(n - 1 \times \text{sgn}(F_x))$, until a position is reached where the adhesion limit is no longer violated, or the fibre detaches (mode 3) or switches into side contact (mode 4).

For a fibre undergoing detachment (mode 3), the fibre is assumed to first retract from its extended position on the surface to a point in space defined by its current incline angle, θ_{current}:

$$\left.\begin{aligned} x_{\text{tip}} &= x_{\text{root}} - \cos(\theta_{\text{current}})L_o \\ y_{\text{tip}} &= y_{\text{root}} - \sin(\theta_{\text{current}})L_o. \end{aligned}\right\} \tag{5.2}$$

Once retracted, the fibre is assumed to immediately swing back to its initial angle θ_{of}. As the fibre swings back to its initial angle, the contact detection algorithm is once again run to determine whether the fibre will return to no contact (mode 0) at its initial rest configuration, or if there is an intermediate angle in which the fibre regains tip contact (mode 1), or side contact (mode 4).

During side contact (mode 4), the assumption is made that the bending moments at the tangential point of contact are exceptionally small compared with the bending owing to adhesive and axial forces during contact, and are therefore neglected. The fibre will follow the surface making tangential contact until tip contact is regained (mode 1) or the surface pulls away and the fibre returns to its rest configuration (mode 0).

At the end of each simulation step i, the normal and shear forces from each fibre are summed to find the total array shear, $F_{x\,\text{total}} = \sum F_x$, and normal forces, $F_{y\,\text{total}} = \sum F_y$. The simulation was implemented and run in Matlab (MathWorks, Natick, MA).

6. Comparison of Johnson–Kendall–Roberts and Kendall peel contact models

The simulation was run for inclination angles, $\theta_{of} = 35-85^\circ$, and indentation depths, $\Delta = 2-5$ µm, and with the fibre properties outlined in table 1. Figure 5 shows two example LDP traces for $\theta_{of} = 51^\circ$ and $\Delta = 2$ µm in force space (figure 5*a*,*c*) and time space (figure 5*b*,*d*) with the spherical indenter of radius = 2 cm. As can be seen in both traces, contact forces begin in compression as the fibre array is loaded, and then switch into tensile loading as the drag begins. Forces remain largely the same during the drag phase for both the spherical- and spatula-shaped tips. For the spatula tips (figure 5*a*,*b*), there is greater variation in the force signal owing to the uncorrelated detachment and re-attachment of the fibres as they peel and re-attach to the surface. During unloading, the forces gradually decrease to zero as the fibres are pulled from the surface. The maximum tensile force occurs during the drag phase of the trace (green star). For the hemispherical-shaped tips (figure 5*c*,*d*), as the array is pulled from the surface the tensile force increases to its maximum (green star) before detaching.

For the hemispherical tips using the JKR contact model, we wish to compare the effect of fibre angle inclination and indenter depth on adhesive forces of the system. Figure 6*a* shows the maximum and figure 6*b* the mean forces on the fibre array for the parameters tested. Maximum tensile forces are plotted as absolute values, mean forces are plotted as tensile being negative. Fibre inclination angle θ_{of} can be seen to have a large effect on both the maximum and mean tensile loads, with nearly vertical fibres showing the lowest tensile loads, confirming experimental results [44]. Indentation depth affects only the mean tensile forces, having little effect on the maximum tensile load. This confirms other studies that have pointed to zero preload being a feature of the fibrillar adhesive system [8]. However, indentation depth does have an effect on the mean forces during the drag. Only an indentation depth of $\Delta = 2$ µm shows tensile loads during drag, an exhibition of the frictional adhesion effect common in fibrillar adhesives [31,32]. Beyond this, forces become monotonically more compressive with indentation depth, and as well, friction forces increase.

For the spatula-shaped tips using the Kendall peel model, we plot the forces using the same parameters as above. Figure 7*a* shows the maximum and figure 7*b* the mean forces on the fibre array. For both the mean and maximum normal forces, indentation depth is not a significant factor. However, there is an increasing shear load with increasing indentation depth, likely because at a higher indentation depth, fibres become more inclined and this reduces the peel angle. Initial fibre angle has less of an effect on the

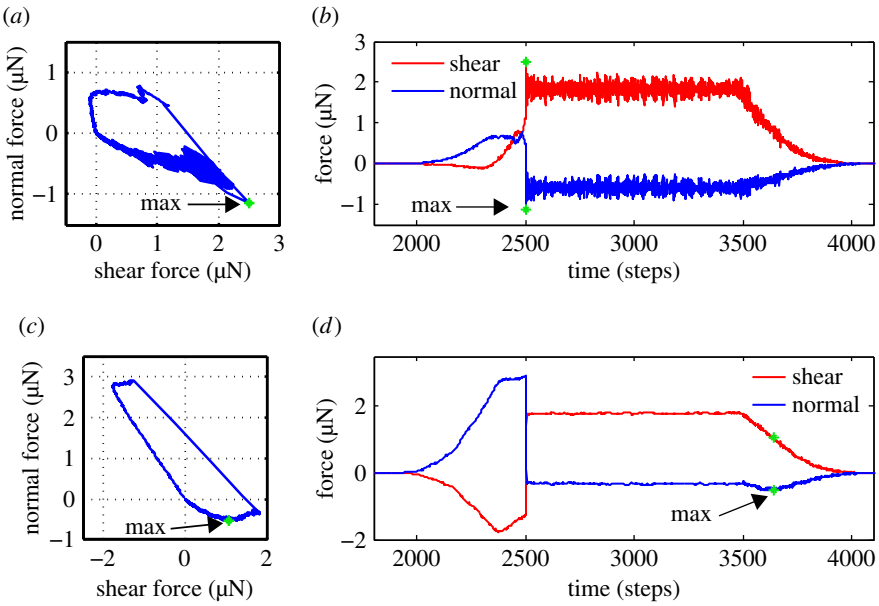

Figure 5. Example load–drag–pull simulation results for 250 fibres with spatula tips using Kendall peel theory plotted in (*a*) force and (*b*) time space, and hemispherical tips using JKR contact theory in (*c*) force and (*d*) time space. The green star indicates the point of maximum tensile load on the array and the corresponding shear load. Each simulation was run on a spherical surface with a radius of 2 cm, an indentation depth of 2 μm and an initial fibre inclination of 51°. (Online version in colour.)

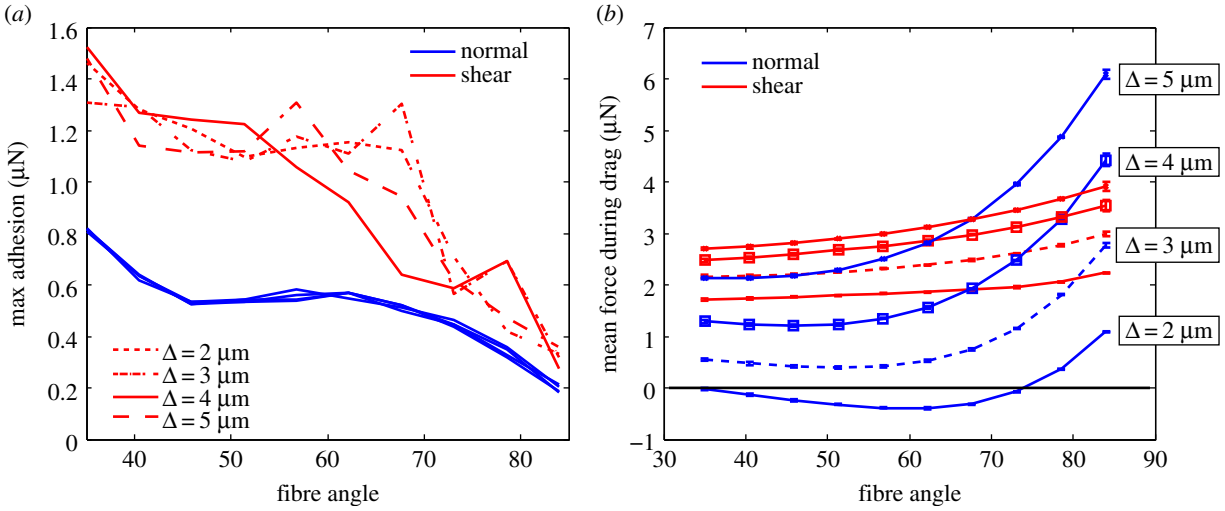

Figure 6. (*a*) Maximum adhesion forces and (*b*) mean forces during drag for an array of 250 fibres with hemispherical tips modelled with JKR theory for surface indentation depths of 2–5 μm on a spherical indenter of radius = 2 cm. Maximum tensile forces are plotted as absolute values, mean forces are plotted as tensile being negative. (Online version in colour.)

maximal normal adhesion; however, for mean adhesion, forces become compressive at angles near vertical similar to the JKR-modelled fibres. For fibres inclined above 60°, forces go from tensile during the drag motion to compressive.

Figure 8 shows a direct comparison of the hemispherical tips and spatula tips for maximal (figure 8*a*) and mean (figure 8*b*) forces at an indentation depth of $\Delta = 3$ μm. For the maximal forces, the spatula-tipped fibres show more than 2.5 times the adhesion across all fibre angles, and about five times the shear, with the largest difference being for nearly vertical fibres. For mean forces during drag, the spatula tips show tensile normal forces, whereas the hemispherical tips remain compressive. Spatula-tipped fibres also show much larger shear loads during the drag for lower-angled fibres. However, for fibres near vertical, both contact models result in fibres that give compressive loads during the drag. Figure 8*c* shows the maximum point of detachment in force space, and the α angle for the JKR and Kendall cases, which represents the maximal force angle at detachment. Red dots represent Kendall data points, whereas blue squares represent JKR data points. The α angle was calculated via the tangent of the corresponding maximum normal and shear forces at pull-off.

Hemispherical-tipped fibres show a maximal α of 25–37°, whereas spatula-tipped fibres have an α of 15–25°. Both these values are approximately the same as the 25° reported for naturally isolated gecko arrays [31,32]. The plot also shows the much larger magnitude of the maximal pull-off force of the spatula-tipped Kendall peel model fibres.

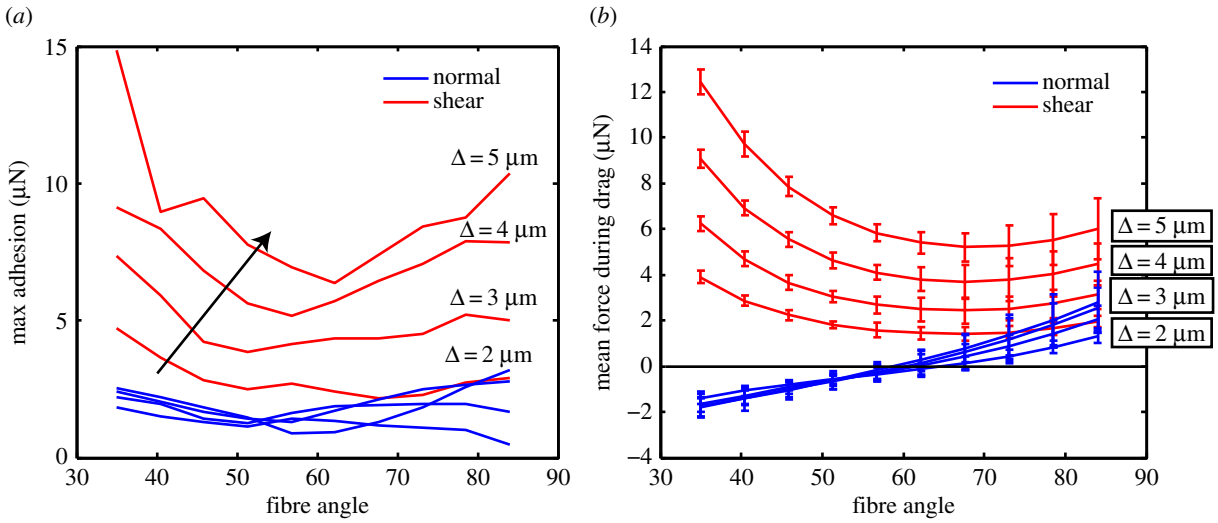

Figure 7. (*a*) Maximum adhesion forces and (*b*) mean forces during drag for an array of 250 fibres with spatula-terminated tips for surface indentation depths of 2–5 μm on a spherical indenter of radius = 2 cm. Maximum tensile forces are plotted as absolute values, mean forces are plotted as tensile being negative. (Online version in colour.)

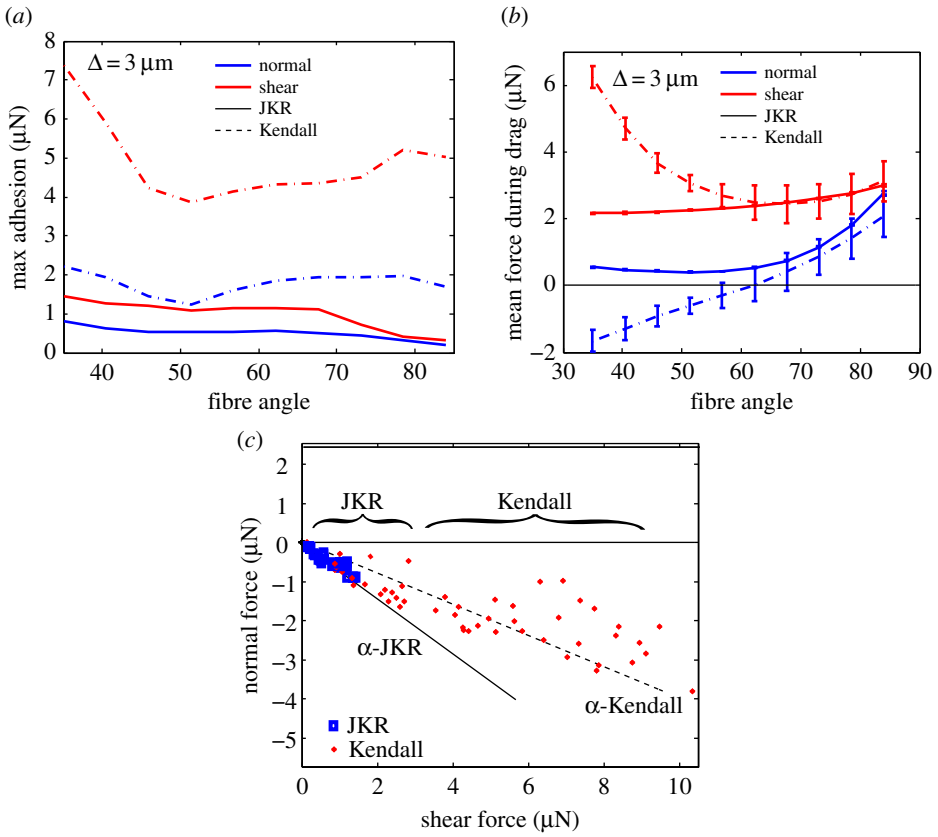

Figure 8. A comparison of the hemispherical tip JKR model fibres and the spatula tip Kendall model fibres for Δ = 3 μm indentation on a spherical indenter of 2 cm radius for (*a*) absolute maximum force, (*b*) mean force during drag and (*c*) maximum pull-off in force space (red dots represent Kendall data points, whereas blue squares represent JKR data points). (Online version in colour.)

The analysis above indicates that on smooth surfaces there is a distinct advantage to spatula terminated fibres in an array. As well, the model shows for the first time that the simple JKR and Kendall contact models, when applied to an array of angled fibres, show very similar behaviour to experimental results on isolated gecko arrays [31,32] and synthetic fibrillar arrays [20]. The cumulative effect of individual fibres acting as Kendall peel is to exhibit behaviour similar to the phenomenological frictional adhesion model presented by Autumn *et al*. [31].

7. Arrays on sinusoidal surfaces

The simulation was run on sinusoidal surfaces of varying amplitudes of 1–5 μm and wavelengths of 1–30 μm, where $y_{\text{surface}} = (A/2)\sin((2\pi/\lambda)x_{\text{surface}})$. Figure 9 shows simulation results for mean forces during drag and maximal adhesion during the trial. As anticipated, at the roughest of surfaces ($A = 5$ μm, $\lambda = 1$ μm), forces drop to near zero, and grow as the wavelength is increased. Above wavelengths of 20 μm, forces level off as the surface is nearly smooth at this point. Mean forces during drag were compressive for

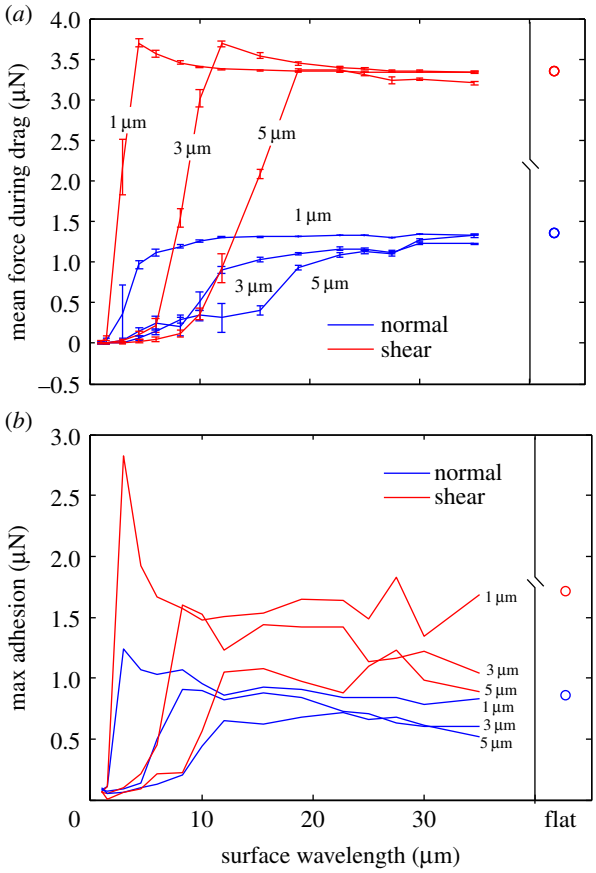

Figure 9. Simulation of 250 hemispherical-tipped JKR array of fibres on sinusoidal surfaces of amplitudes 1–5 μm and wavelengths 1–35 μm showing (*a*) mean normal and shear force during drag and (*b*) absolute maximal adhesion (tensile) during the trial. Fibres have an initial angle of 60°. (Online version in colour.)

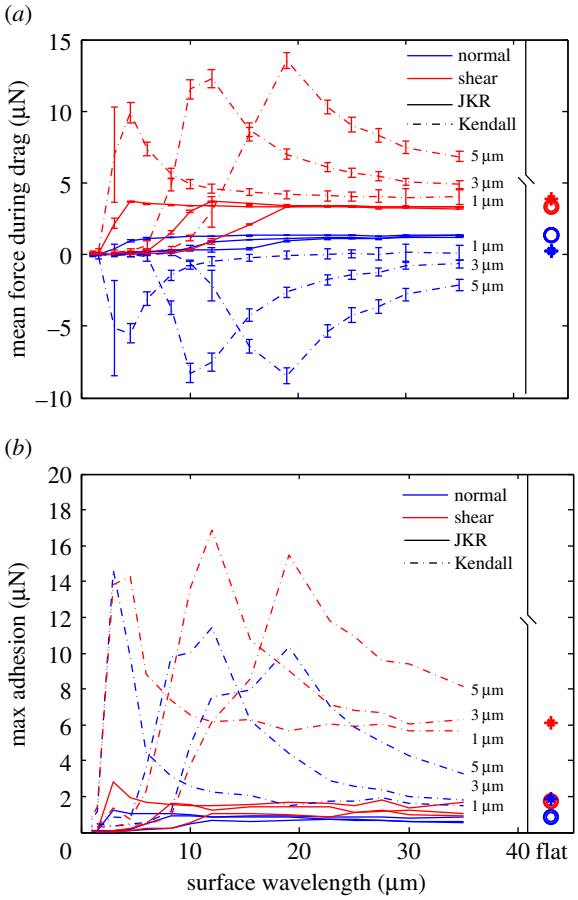

Figure 10. A comparison of the hemispherical tip JKR model fibres and the spatula tip Kendall peel model fibres for sinusoidal surfaces of amplitudes 1–5 μm and wavelengths 1–35 μm showing (*a*) mean normal and shear force during drag and (*b*) absolute maximal adhesion (tensile) during the trial. Fibres have an initial angle of 60°. Adhesive properties of the arrays on a flat surface are marked with star for Kendall and circle for JKR on the far right of the plot. (Online version in colour.)

all surfaces tested, and show that the JKR model does not result in frictional adhesion on the sinusoidal surfaces tested. Interestingly, maximum adhesion shows a higher peak on rougher surfaces (high amplitudes and short wavelengths). This could be due to the local angle of contact, where fibres may actually show a greater resultant force at the surface owing to the favourable angling of the surface. As amplitudes increase, forces begin to fall as the amplitude is large enough to push a significant number of fibres out of contact.

The same surfaces were used to test spatula-tipped Kendall peel model fibres, and a comparison of the spatula-shaped Kendall-modelled tips and hemispherical-shaped JKR-modelled tips is made in figure 10. Spatula-tipped fibres show an order of magnitude larger forces for both mean adhesion and maximal adhesion. As well, mean forces become tensile during the drag phase, and for some amplitudes show larger tensile forces than for the same fibre array on a smooth surface (marked with star for spatula and circle for hemispherical). Interestingly, each amplitude shows a large peak in adhesion at smaller wavelengths. This could be again owing to local surface angle reducing the effective peel angle of the fibre. It has been verified experimentally that local orientation of the seta has a large impact on the adhesive forces [44]. As the surface amplitude increases, so does the wavelength at which this spike in adhesion occurs. As the wavelength of the surface increases, forces converge to the adhesion found on a flat surface.

At the rougher end of the spectrum (high amplitudes and short wavelengths), adhesion drops to nearly zero for wavelengths less than 5 μm at amplitudes of 5 μm. This indicates the critical level of roughness beyond which adhesion is not possible.

8. Discussion

Although many studies have clearly shown the benefit of a spatula terminal feature for adhesion on surfaces with nanoscale roughness, our model shows the efficacy of spatula tips on larger microscale fibre-level roughness. The spatula feature aids in adhesion on surfaces with asperities much larger than the spatula itself (200 nm spatula plate on 5 μm surface amplitude), and exhibits adhesive forces 10 times larger than hemispherical-tipped fibres. However, there is a roughness limit beyond which the spatula no longer aids in adhesion, showing the need for a hierarchical system that would enable conformation to larger asperities. This is similar to experimental results from testing live Tokay geckos on macroscopic sinusoidal surfaces, which showed a loss of adhesion once surface amplitude exceeded gecko toe size [11].

It appears that spatula tips modelled using the Kendall peel equation, when acting in concert through an array of fibres, show the frictional adhesion effect previously described in the literature [31,32]. Important to note is that the spatula-tipped fibres are able to generate tensile loads during the drag phase of the cycle. This is in contrast to the

compressive loads seen in the hemispherical-tipped fibres, and could explain a self-engaging property by which adhered fibres are able to pull more of the array in contact—an effect seen with spatula-shaped natural gecko arrays, but not seen for arrays of synthetic fibres with hemispherical-shaped tips. The analysis shows that even a single hierarchical-level array of fibres could also show this effect on rough surfaces if spatula tips were a feature.

9. Concluding remarks

We sought to understand the impact of surface roughness on the adhesion of two types of GSA arrays: those with hemispherical-shaped tips and those with spatula-shaped tips. Our model showed that the nanoscale geometry of the tip shape alters the macroscale adhesion of the array of fibres by an order of magnitude. On sinusoidal surfaces with amplitudes much larger than the nanoscale features, there is a clear benefit to having spatula-shaped features. Interestingly, fibres acting in concert show behaviour much more complex than what could be predicted with the pull-off model of a single fibre, and both the JKR and Kendall peel models can explain the frictional adhesion effect previously described in the literature when applied to each individual element [31,32]. Similar to experimental results found with the macroscale features of the gecko adhesive system, adhesion drops dramatically when roughness approaches the size and spacing of the fibre features.

This has clear implications for the design of future GSAs that may be used in environments with varying rough surfaces. An integrated approach must be taken that considers the relationship between the surface roughness, the size of the adhesive structures and their ability to conform at a variety of length scales. Understanding the abilities and limitations of these structures on varying length scales of roughness is necessary to create an adhesive that will be effective in a target application.

Acknowledgement. We thank the Biomimetic Millisystems Laboratory.
Funding statement. This work was supported by National Science Foundation NSEC COINS NSF 03-043.

References

1. Peressadko A, Hosoda N, Persson B. 2005 Influence of surface roughness on adhesion between elastic bodies. *Phys. Rev. Lett.* **95**, 124301. (doi:10.1103/PhysRevLett.95.124301)
2. Persson BNJ. 2007 Biological adhesion for locomotion on rough surfaces: basic principles and a theorists view. *MRS Bull.* **32**, 486–490. (doi:10.1557/mrs2007.82)
3. Huber G, Gorb SN, Hosoda N, Spolenak R, Arzt E. 2007 Influence of surface roughness on gecko adhesion. *Acta Biomater.* **3**, 607–610. (doi:10.1016/j.actbio.2007.01.007)
4. Kim TW, Bhushan B. 2007 Adhesion analysis of multi-level hierarchical attachment system contacting with a rough surface. *J. Adhesion Sci. Technol.* **21**, 1–20. (doi:10.1163/156856107779976097)
5. Russell AP, Johnson MK. 2007 Real-world challenges to, and capabilities of, the gekkotan adhesive system: contrasting the rough and the smooth. *Can. J. Zool.* **85**, 1228–1238. (doi:10.1139/Z07-103)
6. Pugno NM, Lepore E. 2008 Observation of optimal gecko's adhesion on nanorough surfaces. *Biosystems* **94**, 218–222. (doi:10.1016/j.biosystems.2008.06.009)
7. Bhushan B. 2007 Adhesion of multi-level hierarchical attachment systems in gecko feet. *J. Adhesion Sci. Technol.* **21**, 1213–1258. (doi:10.1163/156856107782328353)
8. Lee J, Bush B, Maboudian R, Fearing RS. 2009 Gecko-inspired combined lamellar and nanofibrillar array for adhesion on nonplanar surface. *Langmuir* **25**, 12 449–12 453. (doi:10.1021/la9029672)
9. Rodriguez I, Lim CT, Natarajan S, Ho AYY, Van EL, Elmouelhi N, Low HY, Vyakarnam M, Cooper K. 2013 Shear adhesion strength of gecko inspired tapes on surfaces with variable roughness. *J. Adhesion* **89**, 921–936. (doi:10.1080/00218464.2013.767198)
10. Persson BNJ, Gorb S. 2003 The effect of surface roughness on the adhesion of elastic plates with applications to biological systems. *J. Chem. Phys.* **119** 11 437–11 444. (doi:10.1063/1.1621854)
11. Gillies AG, Lin H, Henry A, Ren A, Shiuan K, Fearing RS, Full RJ. 2013 Gecko toe and lamellar shear adhesion on macroscopic, engineered rough surfaces. *J. Exp. Biol.* **217**, 283–289. (doi:10.1242/jeb.092015)
12. Spolenak R, Gorb S, Gao H, Arzt E. 2005 Effects of contact shape on the scaling of biological attachments. *Proc R. Soc. A* **461**, 305–319. (doi:10.1098/rspa.2004.1326)
13. Gorb S, Varenberg M, Peressadko A, Tuma J. 2006 Biomimetic mushroom-shaped fibrillar adhesive microstructure. *J. R. Soc. Interface* **4**, 271–275. (doi:10.1098/rsif.2006.0164)
14. Cheng QH, Chen B, Gao HJ, Zhang YW. 2012 Sliding-induced non-uniform pre-tension governs robust and reversible adhesion: a revisit of adhesion mechanisms of geckos. *J. R. Soc. Interface* **9**, 283–291. (doi:10.1098/rsif.2011.0254)
15. Mergel JC, Sauer RA. 2013 On the optimum shape of thin adhesive strips for various peeling directions. *J. Adhesion* **90**, 526–544. (doi:10.1080/00218464.2013.840538)
16. Greiner C, Spolenak R, Arzt E. 2008 Adhesion design maps for fibrillar adhesives: the effect of shape. *Acta Biomater.* **5**, 597–606. (doi:10.1016/j.actbio.2008.09.006)
17. Kim T, Bhushan B. 2008 The adhesion model considering capillarity for gecko attachment system. *J. R. Soc. Interface* **5**, 319–327. (doi:10.1098/rsif.2007.1078)
18. Hui CY, Glassmaker NJ, Tang T, Jagota A. 2004 Design of biomimetic fibrillar interfaces: 2. Mechanics of enhanced adhesion. *J. R. Soc. Interface* **1**, 35–48. (doi:10.1098/rsif.2004.0005)
19. Gao H, Wang X, Yao H, Gorb S, Arzt E. 2005 Mechanics of hierarchical adhesion structures of geckos. *Mech. Mater.* **37**, 275–285. (doi:10.1016/j.mechmat.2004.03.008)
20. Schubert B, Lee J, Majidi C, Fearing RS. 2008 Sliding-induced adhesion of stiff polymer microfibre arrays. II. Microscale behaviour. *J. R. Soc. Interface* **5**, 845–853. (doi:10.1098/rsif.2007.1309)
21. Majidi C, Groff RE, Fearing RS. 2005 Attachment of fiber array adhesive through side contact. *J. Appl. Phys.* **98**, 103521. (doi:10.1063/1.2128697)
22. Majidi C. 2009 Shear adhesion between an elastica and a rigid flat surface. *Mech. Res. Commun.* **36**, 369–372. (doi:10.1016/j.mechrescom.2008.10.010)
23. Liu J, Hui CY, Shen L, Jagota A. 2008 Compliance of a microfibril subjected to shear and normal loads. *J. R. Soc. Interface* **5**, 1087–1097. (doi:10.1098/rsif.2007.1336)
24. Aksak B, Murphy MP, Sitti M. 2007 Adhesion of biologically inspired vertical and angled polymer microfiber arrays. *Langmuir* **23**, 3323–3332. (doi:10.1021/la062697t)
25. Hui CY, Glassmaker NJ, Jagota A. 2005 How compliance compensates for surface roughness in fibrillar adhesion. *J. Adhesion* **81**, 699–721. (doi:10.1080/00218460500187673)
26. Yao H, Gao H. 2006 Mechanics of robust and releasable adhesion in biology: bottom up designed hierarchical structures of gecko. *J. Mech. Phys. Solids* **54**, 1120–1146. (doi:10.1016/j.jmps.2006.01.002)
27. Chen B, Wu PD, Gao H. 2008 Hierarchical modelling of attachment and detachment mechanisms of gecko toe adhesion. *Proc. R. Soc. A* **464**, 1639–1652. (doi:10.1098/rspa.2007.0350)
28. Yamaguchi T, Gravish N, Autumn K, Creton C. 2009 Microscopic modeling of the dynamics of frictional

adhesion in the gecko attachment system. *J. Phys. Chem. B* **113**, 3622–3628. (doi:10.1021/jp8067415)

29. Gravish N *et al*. 2009 Rate-dependent frictional adhesion in natural and synthetic gecko setae. *J. R. Soc. Interface* **7**, 259–269. (doi:10.1098/rsif.2009.0133)
30. Puthoff J, Holbrook M, Wilkinson M, Jin K, Pesika N, Autumn K. 2013 Dynamic friction in natural and synthetic gecko setal arrays. *Soft Matter* **9**, 4855–4863. (doi: 10.1039/c3sm50267h)
31. Autumn K, Gravish N, Wilkinson M, Santos K, Spenko M, Cutkosky M. 2006 Frictional adhesion of natural and synthetic gecko setal arrays. *Integr. Comp. Biol.* **46**, E5. (doi:10.1093/icb/icj003)
32. Autumn K, Dittmore A, Santos D, Spenko M, Cutkosky M. 2006 Frictional adhesion: a new angle on gecko attachment. *J. Exp. Biol.* **209**, 3569–3579. (doi:10.1242/jeb.02486)
33. Autumn K, Gravish N. 2008 Gecko adhesion: evolutionary nanotechnology. *Phil. Trans. R. Soc. A* **366**, 1575–1590. (doi:10.1098/rsta.2007.2173)
34. Howell LL. 2001 *Compliant mechanisms*, p. 136. New York, NY: John Wiley & Sons, Inc.
35. Tian Y, Pesika N, Zeng H, Rosenberg K, Zhao B, McGuiggan P, Autumn K, Israelachvili J. 2006 Adhesion and friction in gecko toe attachment and detachment. *Proc. Natl Acad. Sci. USA* **103**, 193–205. (doi:10.1073/pnas.0608841103)
36. Gillies AG, Puthoff J, Cohen MJ, Autumn K, Fearing RS. 2013 Dry self-cleaning properties of hard and soft fibrillar structures. *Appl. Mater. Interfaces* **5**, 6081–6088. (doi:10.1021/am400839n)
37. Sitti M, Fearing RS. 2003 Synthetic gecko foot-hair micro/nano-structures as dry adhesives. *J. Adhesion Sci. Technol.* **18**, 1055–1074. (doi:10.1163/15685610332211378 8)
38. Autumn K *et al*. 2002 Evidence for van der Waals adhesion in gecko setae. *Proc. Natl Acad. Sci. USA* **99**, 12 252–12 256. (doi:10.1073/pnas.192252799)
39. Zeng H, Pesika N, Tian Y, Zhao B, Chen Y, Tirrell M, Turner KL, Israelachvili J. 2009 Frictional adhesion of patterned surfaces and implications for gecko and biomimetic systems. *Langmuir* **25**, 7486–7495. (doi:10.1021/la900877h)
40. Johnson KL, Kendall K, Roberts AD. 1971 Surface energy and the contact of elastic solids. *Proc. R. Soc. Lond. A* **324**, 301–313. (doi:10.1098/rspa.1971.0141)
41. Gracias DH, Somorjai GA. 1998 Continuum force microscopy study of the elastic modulus, hardness and friction of polyethylene and polypropylene surfaces. *Macromolecules* **31**, 1269–1276. (doi:10.1021/ma970683b)
42. Endlein T, Ji A, Samuel D, Yao N, Wang Z, Barnes WJ, Federle W, Kappl M, Dai Z. 2013 Sticking like sticky tape: tree frogs use friction forces to enhance attachment on overhanging surfaces. *J. R. Soc. Interface* **10**, 20120838. (doi:10.1098/rsif.2012.0838)
43. Kendall K. 1975 Thin-film peeling: the elastic term. *J. Phys. D, Appl. Phys.* **8** 1449–1452. (doi:10.1088/0022-3727/8/13/005)
44. Hill GC, Soto DR, Peattie AM, Full RJ, Kenny TW. 2011 Orientation angle and the adhesion of single gecko setae. *J. R. Soc. Interface* **8**, 926–933. (doi:10.1098/rsif.2010.0720)